




Thickness dependence of magnetotransport properties of tungsten ditellurideXurui Zhang,^{1,*} Vivek Kakani ¹, John M. Woods,² Judy J. Cha ² and Xiaoyan Shi ^{1,†}¹*Department of Physics, The University of Texas at Dallas, Richardson, Texas 75080, USA*²*Department of Mechanical Engineering and Materials Science, Yale University, New Haven, Connecticut 06511, USA*

(Received 30 April 2021; revised 6 October 2021; accepted 6 October 2021; published 13 October 2021)

We investigate the electronic structure of tungsten ditelluride (WTe₂) flakes with different thicknesses in magnetotransport studies. The temperature-dependent resistance and magnetoresistance (MR) measurements both confirm the breaking of carrier balance induced by thickness reduction, which suppresses the “turn-on” behavior and large positive MR. The Shubnikov-de-Haas oscillation studies further confirm the thickness-dependent change of electronic structure of WTe₂ and reveal a possible temperature-sensitive electronic structure change. Finally, we report the thickness-dependent anisotropy of the Fermi surface, which reveals that multilayer WTe₂ is an electronic 3D material and the anisotropy decreases as thickness decreases.

DOI: [10.1103/PhysRevB.104.165126](https://doi.org/10.1103/PhysRevB.104.165126)**I. INTRODUCTION**

Tungsten ditelluride (WTe₂), a layered transition metal dichalcogenide (TMD) material, has attracted a great deal of interest due to its unique electronic transport properties since the discovery of the nonsaturating positive large magnetoresistance (MR) in bulk [1]. It is widely believed that the extraordinary MR comes from the nearly perfect balance between electron and hole concentrations [1–7]. Many other peculiar electronic properties have also been observed in WTe₂ in transport measurements, such as “turn-on” behavior [1,8–10], multi-Fermi pockets revealed by Shubnikov-de-Haas (SdH) oscillations [11–13], surprisingly small Fermi surface anisotropy [4], ferroelectricity [14–17], superconductivity [18–20], etc. WTe₂ is also a topological material. In the bulk form, WTe₂ has been predicted [21] and observed [22] to be a type-II Weyl semimetal. In the monolayer form, WTe₂ is a quantum spin Hall insulator [23,24] at low carrier density (n). However, it is still unclear how the topological property and the electronic structure evolve by reducing the crystal thickness.

Here we investigate the evolution of electronic structure in WTe₂ flakes with different thicknesses by performing temperature dependent resistance (R - T) measurements, MR measurements, SdH oscillation studies and angle-dependent MR measurements. Experiments show that the imbalance of carrier densities caused by thickness reduction plays an important role in the suppression of the “turn-on” behavior and the large positive MR, while the nonsaturating characteristic was hardly affected. We further confirm that the multilayer WTe₂ is also an electronic 3D material like the bulk crystal and that the anisotropy reduces as thickness decreases.

II. EXPERIMENT

WTe₂ flakes with different thicknesses were obtained by mechanical exfoliation of bulk WTe₂ crystals synthesized by chemical vapor transport [9]. Six exfoliated flakes characterized in this paper can be classified into three groups. The first group contains two thick samples (denoted as sample 1 and sample 2 hereafter) with thickness around 150 nm, the second group contains three thin flakes with thickness around 20 nm (denoted as sample 3 through sample 5 hereafter), and the third group contains one ultrathin flake with thickness at 5 nm (sample 6), whose transport properties have been reported elsewhere [25]. In this paper, we will focus on the first two groups. The thick flakes are directly transferred onto silicon substrates with 285-nm-thick SiO₂ coating on the surface. The thin flakes were encapsulated between two pieces of hexagonal boron nitride (hBN) thin flakes which were about 10 nm thick and transferred onto the substrates by a dry transfer technique [26]. Thin WTe₂ flakes get oxidized easily upon exposure to air [18,27]. Hence the hBN flakes are necessary here to protect the thin samples from air-induced degradation. In addition, hBN flakes provide a cleaner interface for WTe₂. For the thick samples, photo-lithography was used to make the patterns. For the thin samples, electron-beam lithography was used to make patterns. The Ohmic contacts were deposited by electron-beam evaporation of Pd/Au (10 nm/200 nm for thick samples, 10 nm/40 nm for thin samples) followed by a lift-off process. Transport measurements down to 0.02 K were carried out in an Oxford dilution refrigerator. Both the longitudinal resistance R_{xx} and Hall resistance R_{xy} were measured simultaneously by using standard low frequency lock-in techniques.

III. R - T CHARACTERISTICS AND ‘TURN-ON’ BEHAVIOR

Except in the ultrathin sample, the temperature-dependent longitudinal resistances (R - T) in all other five devices (samples 1–5) with different thicknesses show metallic properties across the full experiment temperature range, as shown in

*zxx150430@utdallas.edu

†xshi@utdallas.edu

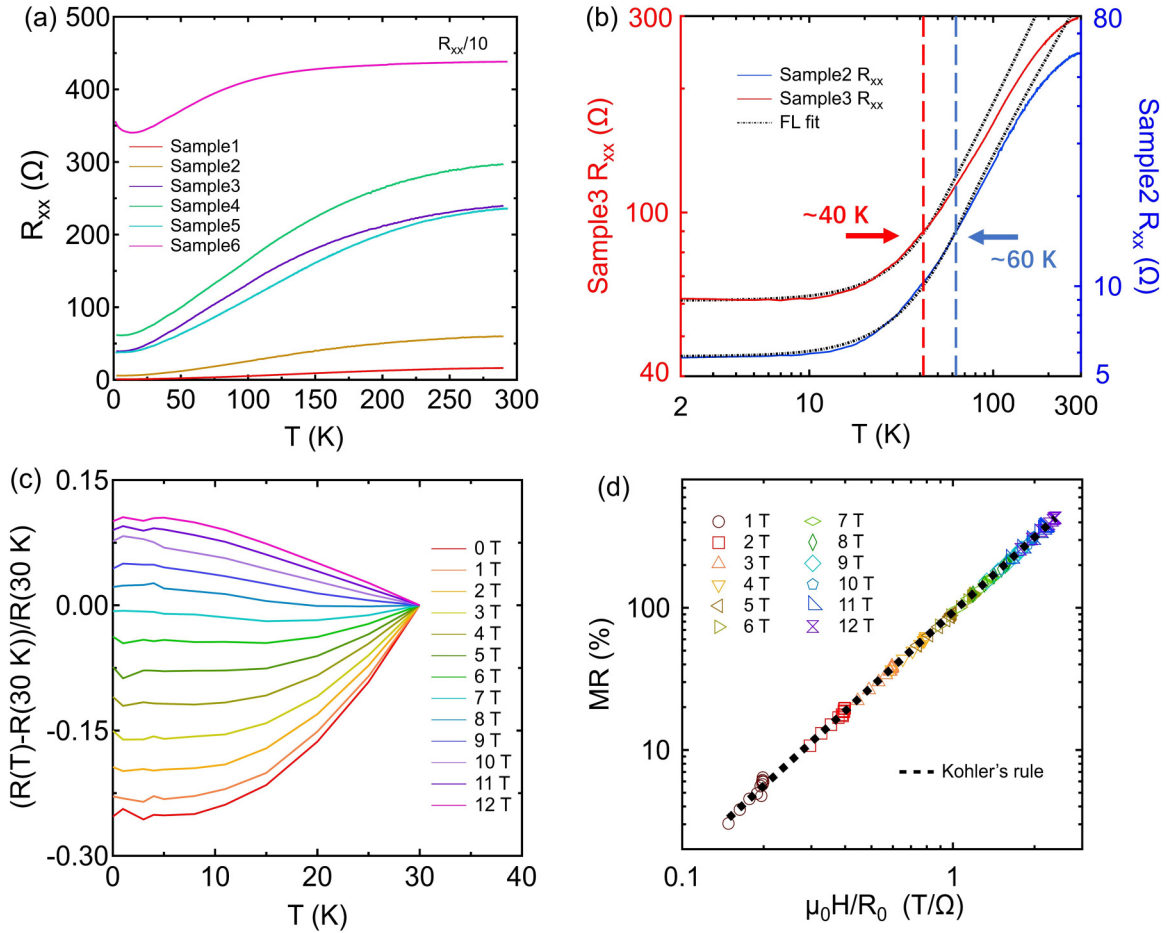


FIG. 1. Temperature-dependent resistance measurements. (a) R - T curves of six different devices. Five of them (samples 1–5) show metallic behavior. (b) Fermi liquid fits (dashed lines) for samples 2 and 3, respectively, at low temperature regions. The upper limits of the Fermi liquid regions are marked with colored dashed lines and arrows. (c) $(R(T) - R(30 \text{ K}))/R(30 \text{ K})$ curves at various magnetic fields manifest “turn-on” behavior in sample 2. (d) Kohler’s rule scaling of the data in (c).

Fig. 1(a). The ultrathin sample (sample 6), however, shows an insulating temperature dependence at low temperature region and it is more than 10 times more resistive than all other samples. All samples in the same group show similar behavior. Thus we pick up samples 2 and 3 as representatives for the thick and thin groups, respectively. In Fig. 1(b), the R - T curves for samples 2 and 3 are plotted in a log-log scale. Fermi liquid fits, $R_0 = \alpha + \beta T^2$, applied at low temperatures are also shown as the black dashed lines for both samples. Here R_0 represents the resistance at 0 T magnetic field and α, β are two fitting parameters. We found that the maximum applicable T of the Fermi liquid fit decreased from ~ 60 K in sample 2 to ~ 40 K in sample 3 with decreasing thickness. Comparing with the case in bulk (~ 80 K) [8], the trend shows consistently that the applicable T range decreases with thickness decreasing.

We further investigated the R - T curves at various magnetic fields up to 12 T. We unambiguously observed the “turn-on” behavior in sample 2, as shown in Fig. 1(c), in which $(R(T) - R(30 \text{ K}))/R(30 \text{ K})$ is plotted as a function of T below 30 K. The R - T curves gradually change from metallic to insulating with magnetic field increasing from 0 T to 12 T. The critical field $\mu_0 H^*$ is around 7 T, which is much larger than the one reported in bulk (below 2 T) [1,8,9]. Due to the

fact that the “turn-on” behavior only occurs in the Fermi liquid state [8,28], we assume that the larger H^* in our case is caused by the shift of the Fermi liquid state to a lower temperature region due to the thickness decreasing. Our assumption can be supported by a comparison measurement in sample 3. In sample 3, the “turn-on” behavior can’t be observed up to 12 T. In a higher field, SdH oscillations emerge and disguise the “turn-on” behavior. That means a magnetic field larger than 12 T is required to manifest the “turn-on” behavior with the Fermi liquid state further moving to a lower temperature region (below 40 K).

In order to investigate the origin of the “turn-on” behavior, we applied Kohler’s rule:

$$\text{MR} = A(H/R_0)^m \quad (1)$$

in which R_0 is the resistance of R - T curve at zero magnetic field and A, m are the constant fitting parameters. Here MR is defined as $\text{MR} = [R(T, H) - R_0(T)]/R_0(T)$. We found that the R - T curves in Fig. 1(c) can be scaled into one curve. Specifically, the Kohler’s rule fitting gave the parameter $m = 1.8$. Comparing with the case in bulk ($m = 1.92$) [8], m decreased and deviated further from the perfect carrier compensation of $m = 2$ [29–31]. The scaling behavior obtained by Kohler’s rule confirmed that the R - T curves at different

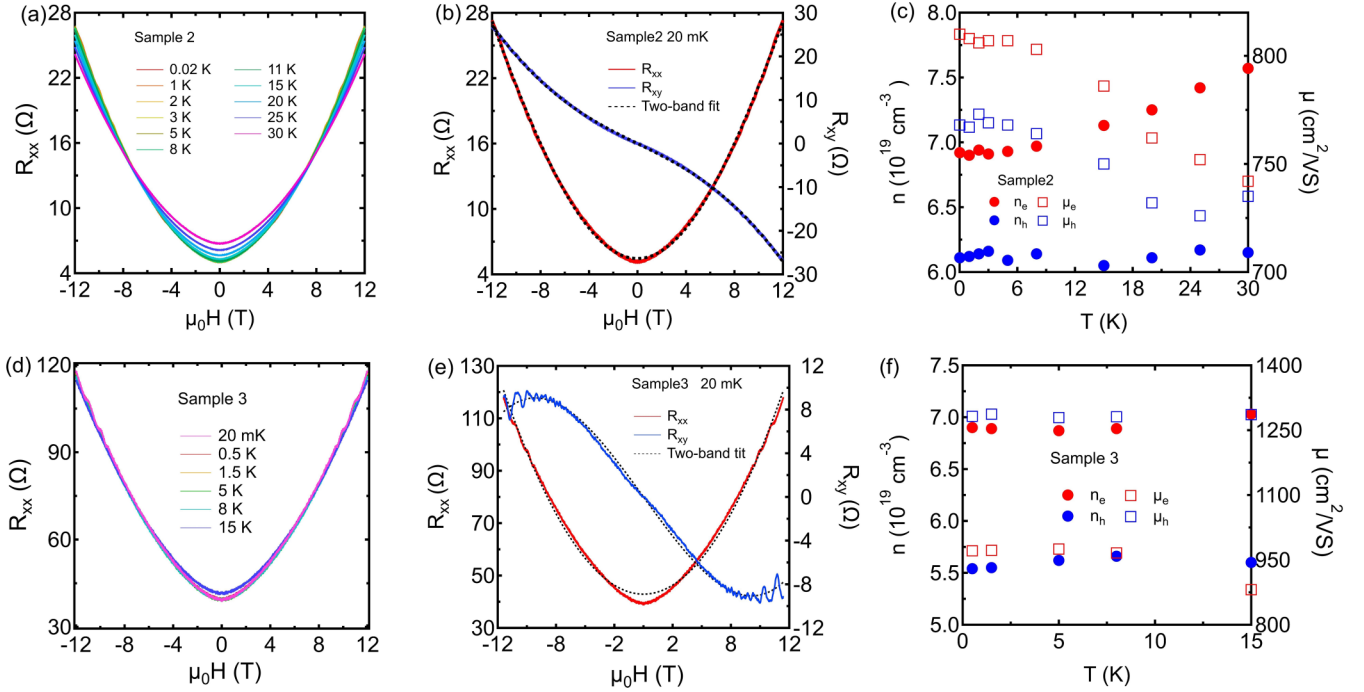


FIG. 2. Magnetoresistances and two-band model fittings in samples 2 and 3. (a) MR curves of sample 2 at various temperatures. (b) A representative two-band model fitting result for sample 2 at 20 mK. (c) Carrier densities (solid circles) and mobilities (open squares) for both electrons (red) and holes (blue) extracted from two-band model fittings at different temperatures for sample 2. (d) MR curves of sample 3 at various temperatures. (e) A representative two-band model fitting result for sample 3 at 20 mK. (f) Carrier densities (solid circles) and mobilities (open squares) for both electrons (red) and holes (blue) extracted from two-band model fittings at different temperatures for sample 3.

magnetic fields have the same temperature dependence, although it looks like the curve at higher field shows larger MR effect. This is quite different from the case of a magnetic field-induced metal-insulator transition, which requires a larger increasing rate at a higher magnetic field due to gap opening [28,32]. In addition, our results show that the “turn-on” behavior takes its origin from carrier compensation. The nearly broken carrier compensation in sample 3 ($m = 1.69$) makes the “turn-on” behavior almost invisible even at 12 T.

IV. TWO-BAND MODEL FITTINGS

To further confirm whether perfect carrier compensation is related to the “turn-on” behavior or not, we performed MR measurements on both samples. The MR curves of both samples at different temperatures are shown in Figs. 2(a) and 2(d). We found that the MR curves in sample 2 crossed at two points located at 7 and -7 T, respectively. This is consistent with the $\mu_0 H^*$ of the “turn-on” behavior. However, it’s almost impossible to identify such two crossing points in sample 3 since the MR curves at different temperatures are fully overlapped in large magnetic field region. This is also consistent with the fact that we didn’t observe obvious “turn-on” behavior in sample 3.

Quasiquadratic positive MR can be seen in both samples, which has been attributed to the perfectly balanced electron and hole densities [3–7,9]. Comparing with the results in bulk [1], which recorded MR as high as 13 000 000%, the highest MR in our samples only showed 1200% due to reduction in thickness. The MR in both samples is notably

suppressed, which indicates an imperfect balance between carrier densities and more impact from defects. But there’s still no observed trend towards saturation of MR in the samples. In order to examine the balance between carrier densities further, we additionally performed Hall measurements. Combined with MRs, we could extract the carrier densities and mobilities using the two-band model [33–35]:

$$R_{xx} = \frac{\sigma_1 + \sigma_2 + (\sigma_1 \sigma_2^2 R_{H_2}^2 + \sigma_2 \sigma_1^2 R_{H_1}^2) B^2}{(\sigma_1 + \sigma_2)^2 + \sigma_1^2 \sigma_2^2 (R_{H_1} + R_{H_2})^2 B^2}, \quad (2)$$

$$R_{xy} = \frac{R_{H_1} \sigma_1^2 + R_{H_2} \sigma_2^2 + \sigma_1^2 \sigma_2^2 R_{H_1} R_{H_2} (R_{H_1} + R_{H_2}) B^2}{(\sigma_1 + \sigma_2)^2 + \sigma_1^2 \sigma_2^2 (R_{H_1} + R_{H_2})^2 B^2}, \quad (3)$$

in which $\sigma_i = n_i e \mu_i$ ($i = 1, 2$) are the conductance contributions from electron and hole, respectively. $R_{H_i} = 1/n_i e$ ($i = 1, 2$) are the Hall coefficients for electron-dominant and hole-dominant Hall effect. n_i and μ_i are carrier densities and mobilities, respectively. The fitting results and the extracted carrier densities and mobilities are shown in Fig. 2.

The two-band model was perfectly applicable to our MR and Hall measurements for sample 2, while there is a little mismatch in the low field region of MR for sample 3 [Fig. 2(e)]. The low-field mismatch might come from the disorder-induced quantum interference effect [25,36–38], which is more pronounced in ultrathin sample where weak localization and weak antilocalization effects are stronger. However, this small mismatch does not have decisive influence on the extraction of carrier densities and mobilities. In sample 2, we found that the hole density was almost unchanged with temperature while the electron density gradually

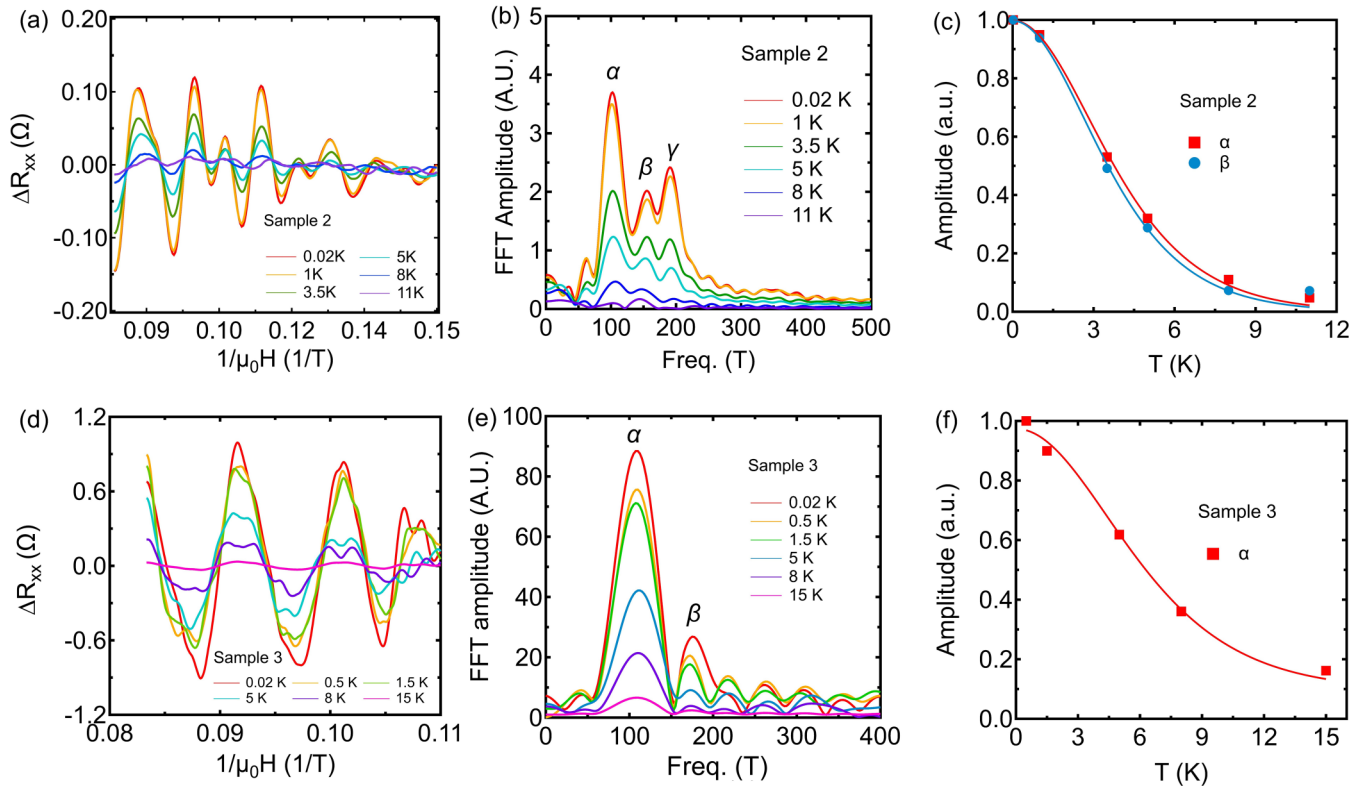


FIG. 3. Temperature dependence of SdH oscillations. (a) SdH oscillations extracted from the MR curves for sample 2. (b) FT analysis shows three peaks corresponding to three Fermi pockets in sample 2, which are marked as α , β , and γ . (c) Temperature dependence of the amplitude of oscillation peaks (square and circle symbols) and the LK fit (solid lines) in sample 2. (d) SdH oscillations extracted from the MR curves for sample 3. (e) FT analysis shows two peaks corresponding to two Fermi pockets in sample 3, which are marked as α and β . (f) Temperature dependence of the amplitude of oscillation peaks (circle symbols) and the LK fit (solid lines) in sample 3.

increases with temperature increasing [Fig. 2(c)]. Such a trend is consistent with other transport and ARPES studies [3–7]. However, the electron and hole densities are not completely equal at low temperature in our samples. The charge carrier density ratio, n_e/n_h , is about 1.15 in sample 2 and becomes even larger in sample 3, which it is 1.26. It indicates that the perfect balance between electron and hole carrier densities will be gradually broken as the thickness decreases. Furthermore, such a growing charge imbalance will cause the MR to be continuously suppressed and will also cause the “turn-on” behavior to become insignificant and eventually disappear. However, it seems that the MR can still maintain the nonsaturating characteristic at large field up to 12 T, no matter how much the MR is suppressed. While the MR in some imbalanced-carrier systems tends to saturate eventually at high magnetic fields [39,40], it is not observed in our experiments. This could be attributed to the fact the either the magnetic field used in our experiment is not large enough or the origin of the nonsaturating characteristic is not the perfect balance of electron and hole compensation. Actually a linear nonsaturating MR has been observed in some Dirac semimetals [41–45], which is believed to take the origin of the lifting of a remarkable protection mechanism induced by time reversal symmetry that strongly suppresses backscatterings at zero magnetic fields. Similar linear MR curves have been observed in disordered WTe_2 flakes [25,46]. A possible link

between the nonsaturating MR in WTe_2 and such a mechanism also deserves further investigation.

It is worth mentioning that both the electron and hole mobilities in sample 2 increased with decreasing temperature, which might be due to the suppression of phonon scattering at lower temperatures. In sample 3, the electron and hole mobilities were larger than those in sample 2 and remained largely unchanged with temperature. This may indicate the mobility enhancement brought about by the encapsulating hBN flakes, which eliminate the interface scattering.

V. SHUBNIKOV DE HAAS OSCILLATIONS

SdH oscillations can be clearly seen in low temperature MR traces [Figs. 2(a) and 2(d)] due to the high carrier mobility and the strong suppression of phonon scattering at low temperatures. The SdH oscillations were extracted from the MR curves by removing the quasiquadratic backgrounds. The extracted oscillations at different temperatures are shown in Figs. 3(a) and 3(d) for sample 2 and sample 3, respectively. Fig. 3(b) and 3(e) shows the corresponding Fourier transformation (FT) analysis. There were three obvious peaks observed in sample 2 and two peaks in sample 3. In sample 2, the three peaks are located at 102 T (α), 161 T (β), and 187 T (γ). These peak locations almost stay unchanged with

temperature. In sample 3, one peak located at 113 T and the other one located at 176 T at 0.02 K and relocated to 169 T above 0.02 K. According to the similarity of locations in sample 2, we assigned α to the first peak and β to the second peak.

According to the Onsager relation $F = (\Phi_0/2\pi^2)A_F$, where F is the oscillation frequency, Φ_0 is the flux quantum, the cross-sectional area of each Fermi pocket can be obtained: $A_F = 0.0097, 0.0153, 0.0178 \text{ \AA}^{-2}$ for α, β, γ pockets in sample 2, respectively. And $A_F = 0.0108, 0.0168$ (at 0.02 K) and 0.0159 (above 0.02 K) \AA^{-2} for α and β pockets in sample 3, respectively. It is inaccurate to identify the carrier types of the Fermi pockets based on both the size of each Fermi pocket and the carrier densities obtained from the two-band model fittings, but we can conclude that the electronic structure changes dramatically with thickness. Firstly, the size of the corresponding pockets in the two samples is marginally different. Although in other SdH oscillation studies in WTe_2 , the size of the pockets is not the same due to different sample sources. In our case, samples 2 and 3 are from the same crystal. So such a difference in the size of the Fermi pockets can be attributed to the changes in the Fermi surface topology caused by the finite-size effect [13]. Secondly, one pocket (γ) totally disappears in sample 3. Compared with the bulk, in which four pockets are discovered [11–13], and the gated trilayer sample, in which two pockets are observed [47], the cases in our samples are in an intermediate state and in line with the trend that the smaller the thickness, the fewer the number of pockets. To sum up the two points, the difference could be intrinsically attributed to the size effect caused by the thickness change of the sample, but other effects, like scatterings from impurities [48], strain effect [49,50] cannot be ruled out. Thirdly, the shift of the β pocket with temperature in sample 3 reveals a temperature-sensitive electronic structure of multilayer WTe_2 . This might be due to the Lifshitz transition which has been previously reported in ARPES studies [3,5] and band structure calculations [51] in WTe_2 . Under certain temperatures, the sizes of some carrier pockets dramatically change due to temperature-induced Fermi surface shift. Besides the Fermi pocket topology, a temperature-induced spin splitting can be explicitly observed in sample 3, as shown in Fig. 3(d). The oscillation peaks double-split with increasing temperature, which is contrary to the common belief that the spin splitting only occurs at low temperature and high magnetic field. What happened here might be due to the breaking of spin-orbit coupling (SOC) with increasing temperature. It has been proved that SOC can be strongly suppressed by temperature-related scatterings in WTe_2 [25]. At low temperature, the SOC is strong so that the applied magnetic field is not sufficient to support an observable Zeeman splitting. At higher temperature, the missing or nondominant SOC enables the appearance of the Paschen–Back effect at moderate magnetic field [52–54]. We did not observe splitting in sample 2, which may be because in thicker samples, the scattering is usually weak due to less fabrication caused disorders, so the SOC is still strong enough and preventing a similar splitting.

The Lifshitz-Kosevich (LK) formula is commonly used to analyze the SdH oscillations [55]. The damping factor shown below in the LK formula is used to describe the temperature dependence of the oscillation amplitude,

$$R_T = \frac{2\pi^2 k_B T m^* / \hbar e B}{\sinh(2\pi^2 k_B T m^* / \hbar e B)}, \quad (4)$$

in which k_B is the Boltzmann constant and m^* is the effective mass. Figures 3(c) and 3(f) show the fitting results for the Fermi pockets in samples 2 and 3, respectively. Since the amplitude of the γ peak in sample 2 and δ peak in sample 3 cannot be reliably extracted above 3.5 K and the β peak in sample 3 shifts location, we excluded them from the fitting analysis. The effective mass obtained from fittings are: $m_\alpha = 0.393 m_e$ and $m_\beta = 0.419 m_e$ for sample 2, and $m_\alpha = 0.301 m_e$ for sample 3, where m_e is the free electron mass. We notice that sample 2 shows comparable results with those in bulk, whereas for sample 3, the effective mass is slightly lighter. This might result from the enhanced carrier mobilities due to the encapsulated structure [11,13,56]. In addition, it is worth mentioning that, the mean free path of each sample can be estimated as $l_2 \approx 39 \text{ nm}$ in sample 2 and $l_3 \approx 46 \text{ nm}$ in sample 3 according to $l = \hbar k_F \mu / e$, in which k_F is the Fermi wave vector expressed as $k_F = \sqrt{A_F / \pi}$. This means that, to a certain extent, the sample quality has not deteriorated as the thickness of the sample decreases. The impurity, scattering effect, etc. in these two samples basically maintain the same level.

VI. FERMI SURFACE ANISOTROPY

We further measured the angle-dependent MR curves, as shown in Figs. 4(a) and 4(c) for samples 2 and 3, respectively. θ is the angle between the direction of the magnetic field and the normal direction of the sample, as shown in the inset of Fig. 4(b). It is observed that the nonsaturating positive MR is strongly suppressed when the magnetic field is parallel to the sample surface. Magnetoresistance oscillation study shows that the peaks in the FT spectrum shift with angle, which indicates the Fermi surface anisotropy between the in-plane and out-of-plane directions. So we further investigated the anisotropy of the Fermi surface through the scaling behavior of MR curves. The scaling behavior [4,57,58] can be expressed as

$$R(H, \theta) = R(\epsilon_\theta H) \quad (5)$$

with the scaling factor $\epsilon_\theta = (\cos^{-2} \theta + \gamma^{-2} \sin^{-2} \theta)^{1/2}$. All the MR curves can be scaled into a single curve as shown in Figs. 4(b) and 4(d), respectively, for both samples. Since the sample resistance is directly related to the effective mass by $R = m^* / n e^2 \tau$, where τ is the relaxation time, the scaling behavior of MR can describe the mass anisotropy $m_{\parallel} / m_{\perp}$, which is the γ in the equation. In addition, since m^* manifests the energy band curvature, γ alone can also be used to describe the anisotropy of Fermi surface $k_{\parallel} / k_{\perp}$ [4,58–60].

The scaling factors were obtained for both samples at different angles and plotted in Fig. 4(e). By fitting the scaling factor versus angle, we got the anisotropy parameter $\gamma = 8.08$ and 2.28 in samples 2 and 3, respectively. Interestingly, the anisotropy we got from WTe_2 is much smaller than

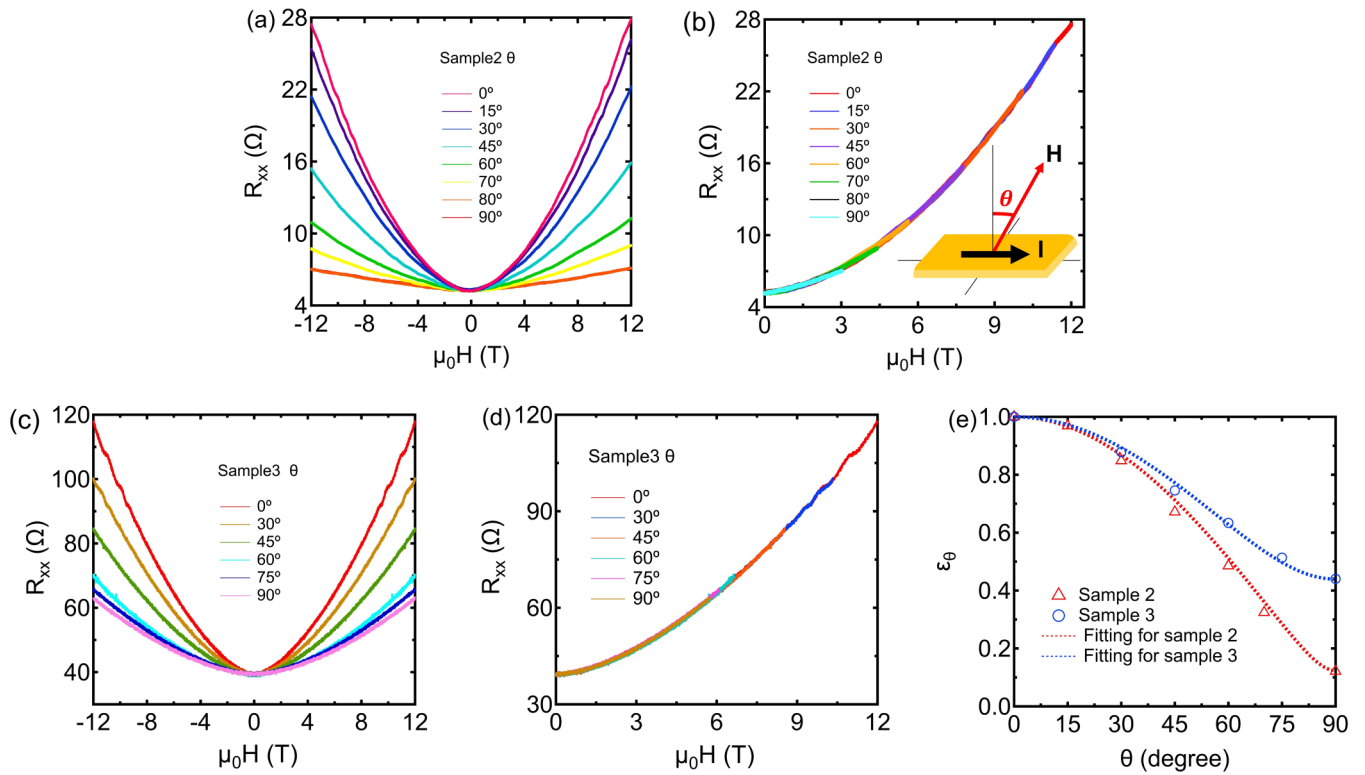


FIG. 4. Angle-dependent MR curves and the scaling behavior. (a) Angle-dependent MR curves in sample 2. (b) The scaling behavior of the MR curves in sample 2. Inset shows the schematic of field orientation. (c) Angle-dependent MR curves in sample 3. (d) The scaling behavior of the MR curves in sample 3. (e) The scaling factors ϵ_θ at different angles (open symbols) and fittings (dotted lines) for both samples.

that in layered material graphite (~ 12) [58], and that in 3D high- T_c superconductor $\text{YBa}_2\text{Cu}_3\text{O}_7$ (~ 9) [61]. Similar small anisotropy in WTe_2 has been experimentally confirmed in several other probes as well [13,62–64]. It is even more striking that the anisotropy parameter in the thick sample is larger than the one in the thin sample. That means the electrons in a thinner WTe_2 sample can move more freely along k_z direction than in a thicker one. Such a small Fermi surface anisotropy indicates that WTe_2 is actually an electronic 3D material. Unlike the isotropic electron gas, however, the electron movement in WTe_2 along the stacking direction is strongly modulated by sample thickness. When the thickness reduces to dozens of nanometers, a thinner sample may suffer less interlayer scatterings along the stacking direction, thereby making the motion of electrons in this direction less constrained. Overall, the multilayer WTe_2 is an electronic 3D material with even smaller anisotropy than that in bulk. This novel evolution of the Fermi surface anisotropy demands further investigations in few-layer or even monolayer materials.

VII. CONCLUSION

With a thorough magnetotransport study in a series of WTe_2 flakes, we have observed a systematic change of elec-

tronic structure as a function of the thickness. First, we confirmed that the Kohler’s rule is applicable and responsible for the “turn-on” behavior which normally occurs in Fermi liquid state, thereby ruling out the possibility of a metal-insulator transition. Second, we found that the imbalance of carrier densities took an important role on the suppression of “turn-on” behavior and large positive MR, while the non-saturating characteristic was hardly affected. This might hint at some other origins for such a MR. Third, the SdH oscillation studies further shown the important role of thickness on the Fermi surface in WTe_2 and perhaps a temperature-sensitive change in electronic structure. Finally, we reported a thickness-dependent Fermi surface anisotropy, which revealed that WTe_2 , a typical 2D Van der Waals material, is effectively an electronic 3D material and the anisotropy decreases with decreasing thickness.

ACKNOWLEDGMENTS

We would like to thank Michael Kolodrubetz for reading and commenting the manuscript. This work was supported by UT Dallas SPIRe fund (No. 2108630). Synthesis of WTe_2 crystals was supported by DOE Basic Energy Sciences (BES) Contract No. DE-SC0014476.

[1] M. N. Ali, J. Xiong, S. Flynn, J. Tao, Q. D. Gibson, L. M. Schoop, T. Liang, N. Haldolaarachchige, M. Hirschberger, N. P.

Ong *et al.*, Large, non-saturating magnetoresistance in WTe_2 , *Nature (London)* **514**, 205 (2014).

- [2] P. S. Alekseev, A. P. Dmitriev, I. V. Gornyi, V. Y. Kachorovskii, B. N. Narozhny, M. Schütt, and M. Titov, Magnetoresistance in Two-Component Systems, *Phys. Rev. Lett.* **114**, 156601 (2015).
- [3] I. Pletikosić, M. N. Ali, A. V. Fedorov, R. J. Cava, and T. Valla, Electronic Structure Basis for the Extraordinary Magnetoresistance in WTe_2 , *Phys. Rev. Lett.* **113**, 216601 (2014).
- [4] L. R. Thoutam, Y. L. Wang, Z. L. Xiao, S. Das, A. Luican-Mayer, R. Divan, G. W. Crabtree, and W. K. Kwok, Temperature-Dependent Three-Dimensional Anisotropy of the Magnetoresistance in WTe_2 , *Phys. Rev. Lett.* **115**, 046602 (2015).
- [5] Y. Wu, N. H. Jo, M. Ochi, L. Huang, D. Mou, S. L. Bud'ko, P. C. Canfield, N. Trivedi, R. Arita, and A. Kaminski, Temperature-Induced Lifshitz Transition in WTe_2 , *Phys. Rev. Lett.* **115**, 166602 (2015).
- [6] Y. M. Dai, J. Bowlan, H. Li, H. Miao, S. F. Wu, W. D. Kong, P. Richard, Y. G. Shi, S. A. Trugman, J. X. Zhu, H. Ding, A. J. Taylor, D. A. Yarotski, and R. P. Prasankumar, Ultrafast carrier dynamics in the large-magnetoresistance material WTe_2 , *Phys. Rev. B* **92**, 161104(R) (2015).
- [7] Y. Luo, H. Li, Y. Dai, H. Miao, Y. Shi, H. Ding, A. Taylor, D. Yarotski, R. Prasankumar, and J. Thompson, Hall effect in the extremely large magnetoresistance semimetal WTe_2 , *Appl. Phys. Lett.* **107**, 182411 (2015).
- [8] Y. L. Wang, L. R. Thoutam, Z. L. Xiao, J. Hu, S. Das, Z. Q. Mao, J. Wei, R. Divan, A. Luican-Mayer, G. W. Crabtree, and W. K. Kwok, Origin of the turn-on temperature behavior in WTe_2 , *Phys. Rev. B* **92**, 180402(R) (2015).
- [9] J. M. Woods, J. Shen, P. Kumaravadivel, Y. Pang, Y. Xie, G. A. Pan, M. Li, E. I. Altman, L. Lu, and J. J. Cha, Suppression of magnetoresistance in thin WTe_2 flakes by surface oxidation, *ACS Appl. Mater. Interfaces* **9**, 23175 (2017).
- [10] M. N. Ali, L. Schoop, J. Xiong, S. Flynn, Q. Gibson, M. Hirschberger, N. P. Ong, and R. J. Cava, Correlation of crystal quality and extreme magnetoresistance of WTe_2 , *Europhys. Lett.* **110**, 67002 (2015).
- [11] P. L. Cai, J. Hu, L. P. He, J. Pan, X. C. Hong, Z. Zhang, J. Zhang, J. Wei, Z. Q. Mao, and S. Y. Li, Drastic Pressure Effect on the Extremely Large Magnetoresistance in WTe_2 : Quantum Oscillation Study, *Phys. Rev. Lett.* **115**, 057202 (2015).
- [12] Z. Zhu, X. Lin, J. Liu, B. Fauqué, Q. Tao, C. Yang, Y. Shi, and K. Behnia, Quantum Oscillations, Thermoelectric Coefficients, and the Fermi Surface of Semimetallic WTe_2 , *Phys. Rev. Lett.* **114**, 176601 (2015).
- [13] F.-X. Xiang, A. Srinivasan, Z. Du, O. Klochan, S.-X. Dou, A. R. Hamilton, and X.-L. Wang, Thickness-dependent electronic structure in WTe_2 thin films, *Phys. Rev. B* **98**, 035115 (2018).
- [14] Z. Fei, W. Zhao, T. A. Palomaki, B. Sun, M. K. Miller, Z. Zhao, J. Yan, X. Xu, and D. H. Cobden, Ferroelectric switching of a two-dimensional metal, *Nature (London)* **560**, 336 (2018).
- [15] P. Sharma, F.-X. Xiang, D.-F. Shao, D. Zhang, E. Y. Tsymbal, A. R. Hamilton, and J. Seidel, A room-temperature ferroelectric semimetal, *Sci. Adv.* **5**, eaax5080 (2019).
- [16] X. Liu, Y. Yang, T. Hu, G. Zhao, C. Chen, and W. Ren, Vertical ferroelectric switching by in-plane sliding of two-dimensional bilayer WTe_2 , *Nanoscale* **11**, 18575 (2019).
- [17] Q. Yang, M. Wu, and J. Li, Origin of two-dimensional vertical ferroelectricity in WTe_2 bilayer and multilayer, *J. Phys. Chem. Lett.* **9**, 7160 (2018).
- [18] V. Fatemi, S. Wu, Y. Cao, L. Bretheau, Q. D. Gibson, K. Watanabe, T. Taniguchi, R. J. Cava, and P. Jarillo-Herrero, Electrically tunable low-density superconductivity in a monolayer topological insulator, *Science* **362**, 926 (2018).
- [19] X.-C. Pan, X. Chen, H. Liu, Y. Feng, Z. Wei, Y. Zhou, Z. Chi, L. Pi, F. Yen, F. Song *et al.*, Pressure-driven dome-shaped superconductivity and electronic structural evolution in tungsten ditelluride, *Nat. Commun.* **6**, 7805 (2015).
- [20] A. Kononov, M. Endres, G. Abulizi, K. Qu, J. Yan, D. G. Mandrus, K. Watanabe, T. Taniguchi, and C. Schönenberger, Superconductivity in type-II Weyl-semimetal WTe_2 induced by a normal metal contact, *J. Appl. Phys.* **129**, 113903 (2021).
- [21] A. A. Soluyanov, D. Gresch, Z. Wang, Q. Wu, M. Troyer, X. Dai, and B. A. Bernevig, Type-II Weyl semimetals, *Nature (London)* **527**, 495 (2015).
- [22] P. Li, Y. Wen, X. He, Q. Zhang, C. Xia, Z.-M. Yu, S. A. Yang, Z. Zhu, H. N. Alshareef, and X.-X. Zhang, Evidence for topological type-II Weyl semimetal WTe_2 , *Nat. Commun.* **8**, 1 (2017).
- [23] S. Wu, V. Fatemi, Q. D. Gibson, K. Watanabe, T. Taniguchi, R. J. Cava, and P. Jarillo-Herrero, Observation of the quantum spin Hall effect up to 100 Kelvin in a monolayer crystal, *Science* **359**, 76 (2018).
- [24] X. Qian, J. Liu, L. Fu, and J. Li, Quantum spin Hall effect in two-dimensional transition metal dichalcogenides, *Science* **346**, 1344 (2014).
- [25] X. Zhang, J. M. Woods, J. J. Cha, and X. Shi, Crossover between weak antilocalization and weak localization in few-layer WTe_2 : Role of electron-electron interactions, *Phys. Rev. B* **102**, 115161 (2020).
- [26] A. Castellanos-Gomez, M. Buscema, R. Molenaar, V. Singh, L. Janssen, H. S. Van Der Zant, and G. A. Steele, Deterministic transfer of two-dimensional materials by all-dry viscoelastic stamping, *2D Mater.* **1**, 011002 (2014).
- [27] L. Wang, I. Gutiérrez-Lezama, C. Barreateau, N. Ubrig, E. Giannini, and A. F. Morpurgo, Tuning magnetotransport in a compensated semimetal at the atomic scale, *Nat. Commun.* **6**, 8892 (2015).
- [28] D. V. Khveshchenko, Magnetic Field-Induced Semimetal-Insulator Transition in Graphite, *Phys. Rev. Lett.* **87**, 206401 (2001).
- [29] E. Sondheimer and A. H. Wilson, The theory of the magnetoresistance effects in metals, *Proc. R. Soc. London A* **190**, 435 (1947).
- [30] M. K. Chan, M. J. Veit, C. J. Dorow, Y. Ge, Y. Li, W. Tabis, Y. Tang, X. Zhao, N. Barišić, and M. Greven, In-Plane Magnetoresistance Obeys Kohler's Rule in the Pseudogap Phase of Cuprate Superconductors, *Phys. Rev. Lett.* **113**, 177005 (2014).
- [31] S. Murzin, S. Dorozhkin, G. Landwehr, and A. Gossard, Effect of hole-hole scattering on the conductivity of the two-component 2D hole gas in GaAs/(AlGa)As heterostructures, *J. Exp. Theor. Phys. Lett.* **67**, 113 (1998).
- [32] Y. Kopelevich, J. M. Pantoja, R. R. Da Silva, and S. Moehlecke, Universal magnetic-field-driven metal-insulator-metal transformations in graphite and bismuth, *Phys. Rev. B* **73**, 165128 (2006).

- [33] N. W. Ashcroft and N. D. Mermin, *Solid State Physics* (Holt, Rinehart and Winston, New York London, 1976).
- [34] F. Rullier-Albenque, D. Colson, A. Forget, and H. Alloul, Hall Effect and Resistivity Study of the Magnetic Transition, Carrier Content, and Fermi-Liquid Behavior in $\text{Ba}(\text{Fe}_{1-x}\text{Co}_x)_2\text{As}_2$, *Phys. Rev. Lett.* **103**, 057001 (2009).
- [35] F. Rullier-Albenque, D. Colson, A. Forget, P. Thuéry, and S. Poissonnet, Hole and electron contributions to the transport properties of $\text{Ba}(\text{Fe}_{1-x}\text{Ru}_x)_2\text{As}_2$ single crystals, *Phys. Rev. B* **81**, 224503 (2010).
- [36] H.-Z. Lu, J. Shi, and S.-Q. Shen, Competition Between Weak Localization and Antilocalization in Topological Surface States, *Phys. Rev. Lett.* **107**, 076801 (2011).
- [37] S. Hikami, A. I. Larkin, and Y. Nagaoka, Spin-orbit interaction and magnetoresistance in the two dimensional random system, *Prog. Theor. Phys.* **63**, 707 (1980).
- [38] H.-Z. Lu and S.-Q. Shen, Finite-Temperature Conductivity and Magnetoconductivity of Topological Insulators, *Phys. Rev. Lett.* **112**, 146601 (2014).
- [39] F. Yang, K. Liu, K. Hong, D. Reich, P. Searson, and C. Chien, Large magnetoresistance of electrodeposited single-crystal bismuth thin films, *Science* **284**, 1335 (1999).
- [40] Y. Kopelevich, J. H. S. Torres, R. R. da Silva, F. Mrowka, H. Kempa, and P. Esquinazi, Reentrant Metallic Behavior of Graphite in the Quantum Limit, *Phys. Rev. Lett.* **90**, 156402 (2003).
- [41] T. Liang, Q. Gibson, M. N. Ali, M. Liu, R. Cava, and N. Ong, Ultrahigh mobility and giant magnetoresistance in the Dirac semimetal Cd_3As_2 , *Nat. Mater.* **14**, 280 (2015).
- [42] Z. Liu, B. Zhou, Y. Zhang, Z. Wang, H. Weng, D. Prabhakaran, S.-K. Mo, Z. Shen, Z. Fang, X. Dai *et al.*, Discovery of a three-dimensional topological Dirac semimetal, Na_3Bi , *Science* **343**, 864 (2014).
- [43] C. Shekhar, A. K. Nayak, Y. Sun, M. Schmidt, M. Nicklas, I. Leermakers, U. Zeitler, Y. Skourski, J. Wosnitza, Z. Liu *et al.*, Extremely large magnetoresistance and ultrahigh mobility in the topological Weyl semimetal candidate NbP, *Nat. Phys.* **11**, 645 (2015).
- [44] N. J. Ghimire, Y. Luo, M. Neupane, D. Williams, E. Bauer, and F. Ronning, Magnetotransport of single crystalline NbAs, *J. Phys.: Condens. Matter* **27**, 152201 (2015).
- [45] S.-Y. Xu, N. Alidoust, I. Belopolski, Z. Yuan, G. Bian, T.-R. Chang, H. Zheng, V. N. Strocov, D. S. Sanchez, G. Chang *et al.*, Discovery of a Weyl fermion state with Fermi arcs in niobium arsenide, *Nat. Phys.* **11**, 748 (2015).
- [46] W. L. Liu, M. L. Chen, X. X. Li, S. Dubey, T. Xiong, Z. M. Dai, J. Yin, W. L. Guo, J. L. Ma, Y. N. Chen *et al.*, Effect of aging-induced disorder on the quantum transport properties of few-layer WTe_2 , *2D Mater.* **4**, 011011 (2016).
- [47] V. Fatemi, Q. D. Gibson, K. Watanabe, T. Taniguchi, R. J. Cava, and P. Jarillo-Herrero, Magnetoresistance and quantum oscillations of an electrostatically tuned semimetal-to-metal transition in ultrathin WTe_2 , *Phys. Rev. B* **95**, 041410(R) (2017).
- [48] M. Busch, O. Chiatti, S. Pezzini, S. Wiedmann, J. Sánchez-Barriga, O. Rader, L. V. Yashina, and S. F. Fischer, High-temperature quantum oscillations of the Hall resistance in bulk Bi_2Se_3 , *Sci. Rep.* **8**, 485 (2018).
- [49] D. Seiler, and K. Hathcox, Effect of uniaxial stress on Shubnikov-de Haas oscillations in HgSe , *Phys. Rev. B* **9**, 648 (1974).
- [50] N. H. Jo, L.-L. Wang, P. P. Orth, S. L. Bud'ko, and P. C. Canfield, Magnetoelastoresistance in WTe_2 : Exploring electronic structure and extremely large magnetoresistance under strain, *Proc. Natl. Acad. Sci.* **116**, 25524 (2019).
- [51] P. Das, D. Di Sante, F. Cilento, C. Bigi, D. Kopic, D. Soranzio, A. Sterzi, J. Krieger, I. Vobornik, J. Fujii *et al.*, Electronic properties of candidate type-II Weyl semimetal WTe_2 . A review perspective, *Electron. Struct.* **1**, 014003 (2019).
- [52] F. Paschen and E. Back, Liniengruppen magnetisch vervollständigt, *Physica* **1**, 261 (1921).
- [53] P. L. Kapitza, P. Strelkov, and E. Laurman, The Zeeman and Paschen-Back effects in strong magnetic fields, *Proc. R. Soc. London A* **167**, 1 (1938).
- [54] M. Abe, R. Itoyama, Y. Komiyama, T. Ito, T. Mashimo, and S. Tojo, Quantitative investigation of the Zeeman and Paschen-Back effects of the hyperfine structure during the rubidium $5^2S_{1/2} \rightarrow 5^2D_{5/2}$ two-photon transition, *Phys. Rev. A* **99**, 053420 (2019).
- [55] D. Shoenberg, *Magnetic Oscillations in Metals* (Cambridge University Press, 2009).
- [56] F.-X. Xiang, M. Veldhorst, S.-X. Dou, and X.-L. Wang, Multiple Fermi pockets revealed by Shubnikov-de Haas oscillations in WTe_2 , *Europhys. Lett.* **112**, 37009 (2015).
- [57] G. Blatter, V. B. Geshkenbein, and A. I. Larkin, From Isotropic to Anisotropic Superconductors: A Scaling Approach, *Phys. Rev. Lett.* **68**, 875 (1992).
- [58] K. Noto and T. Tsuzuku, A simple two-band theory of galvanomagnetic effects in graphite in relation to the magnetic field azimuth, *Jpn. J. Appl. Phys.* **14**, 46 (1975).
- [59] D. Soule, Magnetic field dependence of the Hall effect and magnetoresistance in graphite single crystals, *Phys. Rev.* **112**, 698 (1958).
- [60] D. Soule, J. McClure, and L. Smith, Study of the Shubnikov-de Haas effect. Determination of the Fermi surfaces in graphite, *Phys. Rev.* **134**, A453 (1964).
- [61] T. Ishida, K. Inoue, K. Okuda, H. Asaoka, Y. Kazumata, K. Noda, and H. Takei, Anisotropy of superconductivity in an untwinned $\text{YBa}_2\text{Cu}_3\text{O}_7$ single crystal, *Phys. C: Superconductivity* **263**, 260 (1996).
- [62] Y. Wu, N. H. Jo, D. Mou, L. Huang, S. L. Bud'ko, P. C. Canfield, and A. Kaminski, Three-dimensionality of the bulk electronic structure in WTe_2 , *Phys. Rev. B* **95**, 195138 (2017).
- [63] Y. T. Chan, P. L. Alireza, K. Y. Yip, Q. Niu, K. T. Lai, S. K. Goh, Nearly isotropic superconductivity in the layered Weyl semimetal WTe_2 at 98.5 kbar, *Phys. Rev. B* **96**, 180504(R) (2017).
- [64] R. Bi, Z. Feng, X. Li, J. Niu, J. Wang, Y. Shi, D. Yu, and X. Wu, Spin zero and large Landé g-factor in WTe_2 , *New J. Phys.* **20**, 063026 (2018).